Journal of Materials Chemistry A

Scalable nanomanufacturing of chalcogenide inks: a case study on thermoelectric V–VI nanoplates

Journal:	*Journal of Materials Chemistry A*
Manuscript ID	TA-ART-07-2021-005858.R1
Article Type:	Paper
Date Submitted by the Author:	01-Sep-2021
Complete List of Authors:	Zeng, Minxiang; University of Notre Dame, Aerospace and Mechanical Engineering Xie, Hongyao; Northwestern University Saeidi-Javash, Mortaza; University of Notre Dame, Department of Aerospace and Mechanical Engineering Tanvir, ANM; University of Notre Dame, Aerospace and Mechanical Engineering Du, Yipu; University of Notre dame, Department of Aerospace and Mechanical Engineering Chen, Jiahao; northwestern university, Materials Science and Engineering Zhang, Yanliang; University of Notre dame, Department of Aerospace and Mechanical Engineering Kanatzidis, Mercouri; Northwestern University, Department of Chemistry

SCHOLARONE™
Manuscripts

Scalable nanomanufacturing of chalcogenide inks: a case study on thermoelectric V–VI nanoplates

Minxiang Zeng,[a] Hongyao Xie,[b] Mortaza Saeidi-Javash,[a] Newaz Mohammad Tanvir,[a] Yipu Du,[a] Jiahao Chen,[a] Mercouri G. Kanatzidis,[b] and Yanliang Zhang[a,*]

[a]*Department of Aerospace and Mechanical Engineering, University of Notre Dame, Notre Dame, IN 46556, USA*

[b]*Department of Chemistry, Northwestern University, Evanston, Illinois 60208, United States*

**Corresponding Author:* yzhang45@nd.edu.

ABSTRACT: Solution-processed semiconducting main-group chalcogenides (MMCs) have attracted increasing research interests for next-generation device technologies owing to their unique nanostructures and superior properties. To achieve the full potential of MMCs, the development of highly universal, scalable, and sustainable synthesis and processing methods of chalcogenide particles is thus becoming progressively more important. Here we studied the scalable factors for the synthesis of two-dimensional (2D) V–VI chalcogenide nanoplates (M_2Q_3: M=Sb, Bi; Q=Se, Te), and systematically investigated their colloidal behaviour and chemical stability. Based on a solvent engineering technique, we demonstrated scale-up syntheses of MMCs up to 900% increase of batch size compared with conventional hydrazine-based gram-level syntheses, and such scalable approach is highly applicable to various binary and ternary MMCs. Furthermore, we studied the stability of printable chalcogenides nanoparticle inks with several formulation factors including solvents, additives, and pH values, resulting in inks with high chemical stability (>4 months). As a proof of concept, we applied our solution-processed chalcogenide particles to multiple additive manufacturing methods, confirming the high printability and processability of MMC inks. The ability to combine the top-down designing freedom of additive manufacturing with bottom-up scalable synthesis of chalcogenide particles promises great opportunities for large-scale design and manufacturing of chalcogenide-based functional devices for broad applications.

INTRODUCTION

Main-group chalcogens and metal chalcogenides containing sulfur (S), selenium (Se), or tellurium (Te) are versatile material platforms for energy conversion,[1-3] sensing,[4] and high-speed computing devices.[5, 6] For example, main-group chalcogenides (MMCs) have shown great promises in thermoelectric energy conversion including Bi_2Te_3, Sb_2Te_3, SnSe, and PbTe.[7-9] Some prominent examples of thermoelectric MMCs not only demonstrate excellent figure of merit (*ZT*) by themselves,[10] but also enable promising thermoelectric composites with other additive materials, such as carbon nanotubes.[11, 12] A few MMCs also show intriguing phase-change properties and have been used in phase-change memory (PCM), leading to

the development of solid-state drive and in-memory computing devices with sub-nanosecond writing (*e.g.*, $Sc_{0.2}Sb_2Te_3$).[13] The soft lattices of chalcogenides are both a blessing and curse: on the one hand, this leads to rich phase-transformation behaviors and associated property changes (e.g. electrical resistivity, optical reflectivity) that can be exploited;[16, 17] on the other hand, such changes lead to complexities and uncertainties in their synthesis, in which impurity and undesired phases can occur in large-batch syntheses. Unlike metal oxides that can often be produced via scalable hydrolysis, the synthesis of MMCs often involves toxic ligands or reducing agents (e.g., hydrazine, trioctylphosphine) to convert precursors into chalcogenides and maintain crystallinity with necessity of inert atmospheres, limiting the potential for large-scale application in an industrial environment.

From an industrial nanomanufacturing perspective, an ideal synthesis process should include low cost precursors (stable and commercially available sources), benign starting materials (reagents with medium to low toxicity), and high production yield (minimal impurity to avoid costly separation/purification processes).[18] At an industrial scale, the energy input should also be carefully considered:[19] highly scalable and controllable energy input (such as heat) should be prioritized, while expensive and small-scale energy sources (such as sonication energy) should be avoided. Last but not least, the MMCs should be compatible with scalable device manufacturing techniques (such as additive manufacturing), which facilitates device fabrication from nanoscale building blocks to final products. Despite past efforts focusing on the MMCs nanoparticle performance (e.g., electrical conductivity, band gap, and etc.),[20] the synthesis scalability has rarely been systematically quantified, and more importantly the behavior of chalcogenides dispersion in practical application environments, such as in air and ink phase, is not well understood.

Here, we proposed a bottom-up approach to understand and address the research gap of converting nanoscale MMCs into macroscale devices in the context of scalable manufacturing and solution-based ink processing (**Figure 1a**). We begin with the scalability analysis on different synthesis methods and propose a solvent engineering strategy to minimize the phase impurity during scale-up syntheses. Such scalable manufacturing approach can be generalized for various one-dimensional and two-dimensional

chalcogenide-based systems, including Te nanorods (1.40 ± 0.42 μm in length), Bi_2Te_3 (0.96 ± 0.11 μm), $Bi_2Te_{2.7}Se_{0.3}$ (0.87 ± 0.27 μm), and Bi_2Se_3 (1.14 ± 0.25 μm), as shown in **Figure 1b**. To achieve high ink quality and stability, we investigated the effect of different ink formulations including solvent, pH, and additives on the electrical conductivity of chalcogenide nanoparticles. By optimizing the ink formulation of MMCs, we are able to achieve MMCs nanoplates with long-term chemical stability (>4 months). As a proof of concept, we applied our solution-processed chalcogenide particles to multiple additive manufacturing methods, demonstrating the high printability and processability of the MMC-based inks.

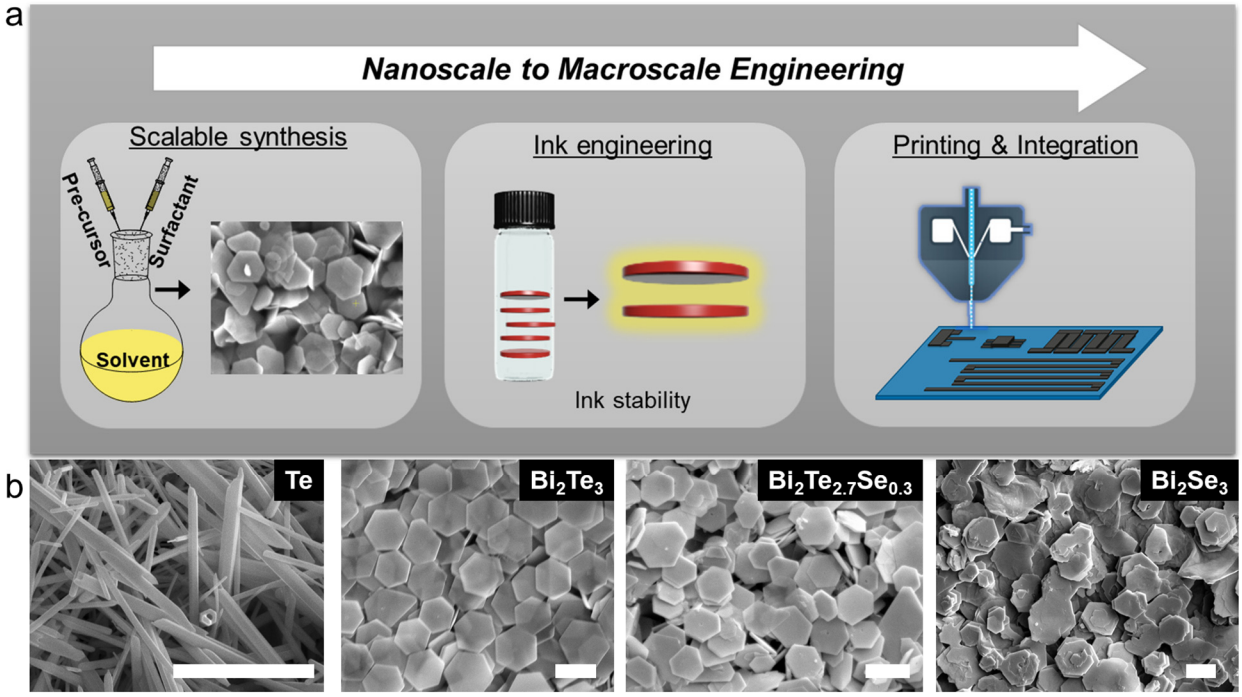

Figure 1. The bottom-up strategy of scalable chalcogenide synthesis for printable inks. (a) Schematic illustration of scalable nanoparticle synthesis, ink engineering, and additive manufacturing. (b) Examples of chalcogens and chalcogenides systems from colloidal synthesis. Scale bars are 1 μm.

We first systematically compared the hydrazine-assisted colloidal synthesis (HCS),[21] ethylene-glycol-assisted colloidal synthesis (ECS),[22] and solvent-engineered colloidal synthesis (SCS) with regard to their scalability (a detailed comparison of these methods can be found in **Table S1**). As a reducing agent, hydrazine has historically been used to synthesize metal chalcogenide nanoparticle from precursors due to

its strong reductive capability and ease of separation (oxidation product of hydrazine is nitrogen gas). Despite previous successes in small-batch Sb_2Te_3 synthesis using toxic hydrazine,[21] we found it quite challenging to scale up the hydrazine-assisted colloidal synthesis as we observed the existence of impurity in final products. As shown in **Figure 2a**, the SEM image of moderate scale-up of HCS leads to significant amount of tellurium nanowire as undesired byproducts. Past studies have suggested that Te is the intermediate product during the Sb_2Te_3 synthesis, where Te can undergoes disproportion in alkali medium to form Te^{2-} which then transforms into Sb_2Te_3 nanoplates.[23, 24] To allow the disproportion reaction proceed to completion, the choice of reaction conditions is important.[25] We tested the reaction procedure with the same starting materials in EG without hydrazine (*i.e.,* ECS method) and surprisingly observed less amount of Te nanowire formed during synthesis (**Figure 2b**). It is worth mentioning that the solvent EG can behave as reducing agent at elevated temperature. Some studies have suggested that ethylene glycol can be oxidized into glycolaldehyde and glycolate.[26, 27] As glycolaldehyde has a lower boiling point of 131.3 °C, an elevated temperature may help the removal of oxidation product glycolaldehyde from the system. According to Le Chatelier's principle, any change in status quo prompts an opposing reaction in the responding system. To further facilitate the reaction, the reaction temperature is elevated by a solvent composition engineering through applying mixed solvents of EG and diethylene glycol (DEG). As shown in SEM image (**Figure 2c**), pure-phase Sb_2Te_3 nanoplates were obtained without observable Te nanowires. Furthermore, X-ray diffraction (XRD) analyses were performed to evaluate the phase purity of Sb_2Te_3 nanoplates by HCS, ECS, and SCS methods. As shown in **Figure 2d**, SCS-synthesized Sb_2Te_3 nanoplates shows almost identical XRD peak pattern as reference XRD from Inorganic Crystal Structure Database (ICSD), whereas there is noticeable Te peak for HCS and ECS methods. In particular, the HCS showed high Te signals with I_{Te}: I_{Sb2Te3} reaching above 1.6 (**Figure 2e**). Although anhydrous EG has a relativity high boiling point of 197 ^{o}C, the EG-based reaction mixture in a scale-up batch shows a lower reflux temperature (under 1 atm) due to the existence of volatile compound (e.g., water produced from reaction). The maximum reaction temperatures of these three methods are recorded, as shown in **Figure 2e**, revealing an opposite trend of increasing reaction temperature vs. impurity amount (Te). This is consistent with the Le Chatelier's

principle, which indicates that a higher reaction temperature facilitates overall chalcogenide conversion by removing the disproportionation reaction product of Na_2TeO_3 through reacting with EG. In addition, we observe that a higher reaction temperature in scale-up SCS also enables the formation of slightly larger particles (1.87 ± 0.40 μm), whereas the particles formed from scale-up HCS and ECS are in size of 1.64 ± 0.41 μm and 0.93 ± 0.17 μm, respectively. These results confirm the critical role of reaction conditions (e.g., solvent and temperature) in scale-up synthesis of metal telluride nanoplates.

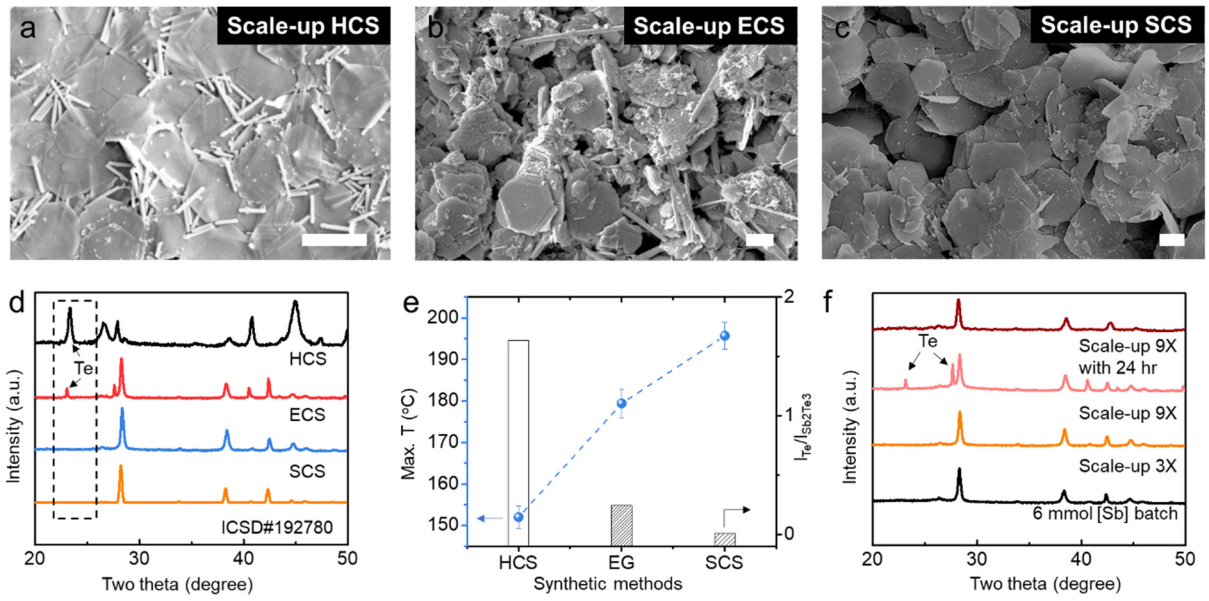

Figure 2. Scalability analyses of different colloidal synthesis approaches. (a-c) SEM images of HCS (a), ECS (b), and SCS (c) at a scale-up batch. (d) XRD of Sb_2Te_3 nanoplates synthesized by HCS, ECS, and SCS approaches. (e) The relationship between maximum reaction temperature and the amount of excess Te (characterized by the ratio of I_{Te}: I_{Sb2Te3}). (f) XRD of Sb_2Te_3 nanoplates at different scales. Scale bars are 1 μm.

To quantify the scalability of SCS approach, we further study the reaction kinetics over different precursor amounts and reaction time. In a small-batch synthesis, a batch of 6 mmol of Sb precursors (e.g., $SbCl_3$) was used to produce around 3 mmol Sb_2Te_3 of nanoplates in 12 h. As shown in XRD data (**Figure 2f**), a 300% scale-up synthesis shows no Te signal, while some impurity starts to emerge as batch size increases to a 900% batch. Nevertheless, such Te impurity can be completely eliminated by prolonging the reaction time to 24 h, leading to an impurity-free synthesis of Sb_2Te_3 nanoplates. In addition to Sb_2Te_3

nanoplates, Bi_2Te_3 shares the same crystal structure (space group R-3m) with Sb_2Te_3 (**Figure 3a**), and thus we hypothesize that such scale-up synthesis can also be applicable to Bi_2Te_3 syntheses. As shown in **Figure 3b**, SEM images reveal a hexagonal morphology of Bi_2Te_3 without any observable Te nanowires, which is confirmed using XRD analysis (shown in **Figure 3c**). Similarly, binary bismuth selenide (Bi_2Se_3) nanoplates have also been prepared with no observable impurity (**Figure S1**). Noticeably, such colloidal synthesis is not limited to binary chalcogenide systems, but also applicable to more sophisticated composition. As a proof of concept of synthesizing ternary chalcogenides, SCS method was employed to prepare pure-phase $Sb_{1.5}Bi_{0.5}Te_3$ (**Figure 3d**) and $Bi_2Te_{2.7}Se_{0.3}$ (**Figure 3e**), where no Te impurity was observed in above systems as evidenced by XRD analyses. Furthermore, to evaluate the transport properties of MMCs, the scale-up synthesized $Bi_2Te_{2.7}Se_{0.3}$ nanoparticles were consolidated into a pellet using spark plasma sintering (SPS) followed by thermoelectric property measurements (**Figure S2**). With a room-temperature electrical conductivity of ~60,000 S m^{-1}, the pellet sample demonstrated a peak *ZT* of 0.7 at 375 K (**Figure 3f**), which are comparable to some wet-chemistry synthesized n-type Bi_2Te_3-based chalcogenides reported in literature.[24, 28, 29]

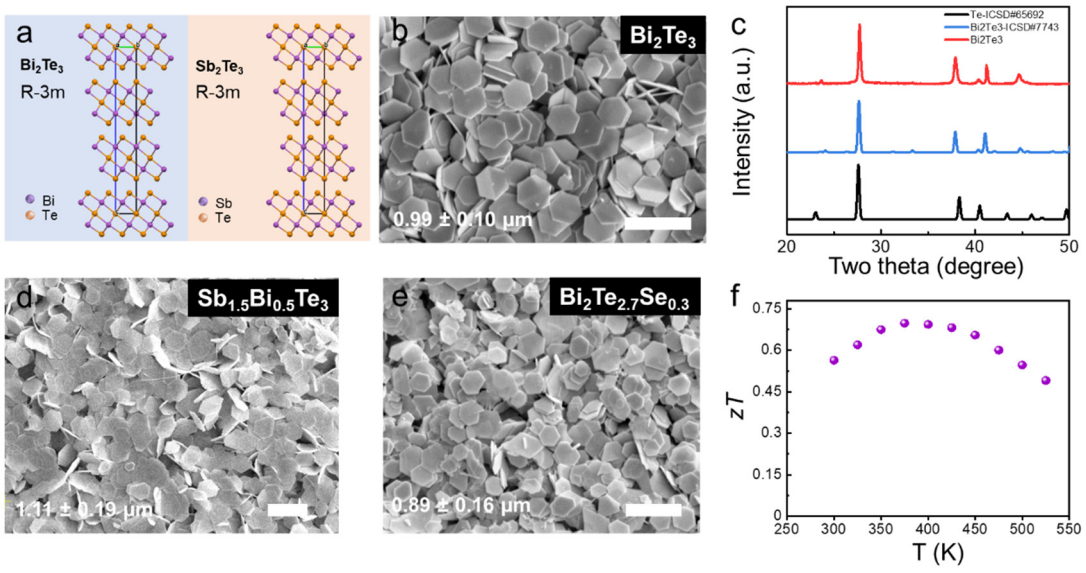

Figure 3. Application of SCS to binary and ternary chalcogenides. (a) Crystal structure of Sb_2Te_3 and Bi_2Te_3 with quintuple-layers. (b) SEM image of Bi_2Te_3 nanoplates made from SCS method. (c) XRD of Bi_2Te_3 nanoplates confirming the pure phase without Te impurity. (d-e) SEM image of ternary chalcogenide $Sb_{1.5}Bi_{0.5}Te_3$ (d) and $Bi_2Te_{2.7}Se_{0.3}$ (e) made from SCS method. (f) Thermoelectric ZT of n-type ternary chalcogenide nanoplates. Scale bars are 2 μm.

To implement chalcogenides inks in additive manufacturing, the ink stability is a crucial factor. We hypothesize that the ink stability depends on several factors including solvents, additives, and pH values, and we further study and optimize ink formulations to prolong the chalcogenide nanoplate's chemical stability (**Figure 4a**). It is worth mentioning that our goal is not to completely prevent the particle oxidation; instead, we aim to qualitatively understand the collective behavior of chalcogenide nanoplates under different ink factors in order to mitigate such oxidation processes. Using $Bi_2Te_{2.7}Se_{0.3}$ as an example, different ink formulations have been systematically investigated including ink solvent, oxygen scavengers, and pH modifiers (**Figure 4b**). We select water as reference ink solvent as it has been widely used in various printing techniques (e.g., inkjet printing).[30] Ethylene glycol is also tested to examine the solvent effect on particle stability. Vitamin C (VC) and ethyl gallate (EGL) are popular oxygen scavengers used in food industry,[31, 32] and thus are also tested in our experiments (vitamin C was neutralized with $NH_3 \cdot H_2O$ to pH of ~7 before adding to chalcogenide system). It has shown that the ink solvent can significantly affect the long-term stability of the inks, where $Bi_2Te_{2.7}Se_{0.3}$ particles in ethylene glycol shows the highest stability, showing 6 times improvement in electrical conductivity than that of the conventional water-based ink formulation. VC-based inks also show good stability and demonstrate the second lowest electrical resistivity. For sample with HCl solution, we observed high resistivity of $Bi_2Te_{2.7}Se_{0.3}$ particles in acidic environment, which suggests acids should be avoided in chalcogenide ink formulation. To our surprise, the EGL-based ink seems to produce relatively resistive films and such high resistivity is likely due to the formation of insulating polymer layer on $Bi_2Te_{2.7}Se_{0.3}$ particles, as evidenced by other polyphenol systems where the oxidation of polyphenol (such as EGL) often leads to oxidative polymerization.[33, 34]

To further understand the stabilization mechanism of EG-based ink formulation, we examined the surface charging group of $Bi_2Te_{2.7}Se_{0.3}$ particles through *in situ* characterization of the surface charge in the ink stage using zeta potential techniques. For freshly made $Bi_2Te_{2.7}Se_{0.3}$ particles, we observed a slightly negative value of -3.52 ± 5.24 mV at neutral pH environment, which is comparable to other chalcogenide nanoplate systems.[35] After long-term storage in water (120 days), we observed the surface potential of

water-based inks sharply plummets to -27.51 ± 2.59 mV (**Figure 4c**), which indicates the formation of negatively charged groups such as -OH.[36-38] By contrast, the EG-based ink only shows a slight decrease in surface potential to -6.58 ± 3.52 mV. In addition, sedimentation analyses of water-based and EG-based inks (**Figure S3**) reveal a fast sedimentation of $Bi_2Te_{2.7}Se_{0.3}$ particles in water-based inks in less than 0.5 h, whereas no observable sedimentation was seen for EG-based inks primarily due to the high viscosity of EG as the sedimentation coefficient is inversely proportional to solvent viscosity. To verify the phase stability of chalcogenide nanoplates, we performed a comparative analysis on the $Bi_2Te_{2.7}Se_{0.3}$ particles before and after long-term storage in EG (4 months). As shown in the XRD data (**Figure 4d**), there is no significant shift in the peak position or new impurity peaks, indicating decent chemical stability of EG-based ink. The improved stability of chalcogenide particles is attributed to the ability of ethylene glycol to effectively quench reactive oxygen species (ROS).[39, 40] In fact, the ethylene glycol has been widely used to reduce metal precursors into metals such as Ag and Pd at room temperature.[41, 42]

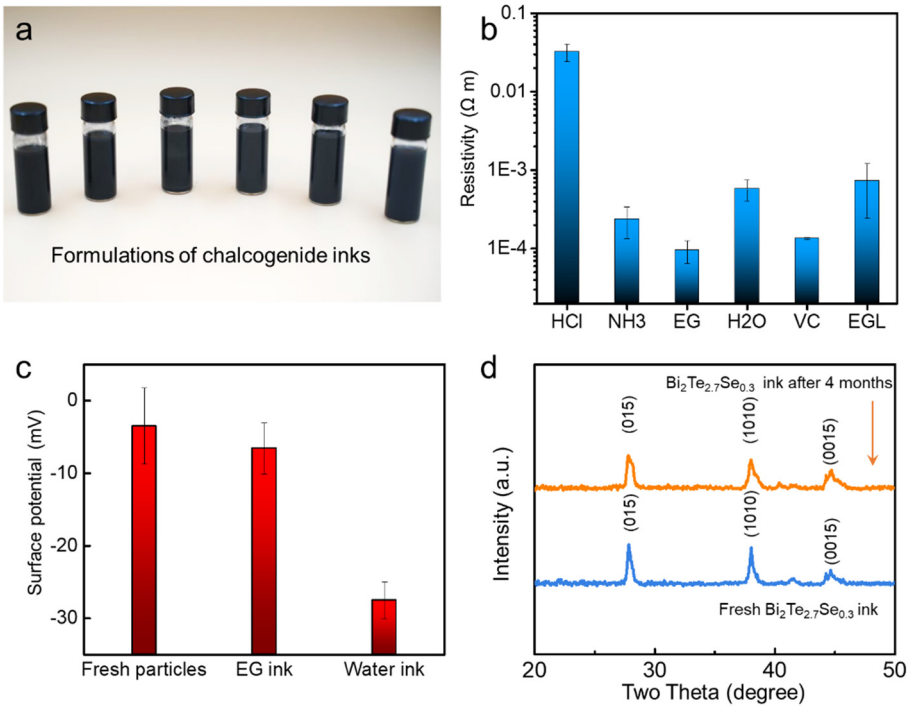

Figure 4. Ink formulations and stability of SCS synthesized MMCs. (a) Photographic image of formulations of various MMCs inks. From left to right is HCl, NH_3, EG, water, vitamin C, ethyl gallate inks. (b) Resistivity of MMC particles stored in various

inks for a period of time (45 days). (c) Zeta potential measurements of fresh ink, EG ink, and water ink of $Bi_2Te_{2.7}Se_{0.3}$ for a period of time (4 months). (d) XRD analysis of fresh and EG ink of $Bi_2Te_{2.7}Se_{0.3}$ for a period of storage time (4 months).

Having demonstrated the long-term stability of EG-based chalcogenide inks, we investigated the compatibility of our inks with different additive manufacturing methods including aerosol jet printing and extrusion printing techniques (**Figure 5a**). We first tested the printability of EG-based inks using extrusion printing. As shown in **Figure S4**, several high-quality films can be readily printed without significant undesired "coffee ring" effect. The printability of inks with high particle concentrations (up to 43 wt%) was tested and no severe clogging was observed due to minimal aggregation or agglomeration of the particles. Despite the intrinsic high viscosity of EG, it is worth mentioning that the EG-based ink can also be printed using other printing methods requiring relatively low ink viscosities by judiciously designing the ink rheology (such as mixing with low viscosity solvents). For example, ultrasonic-based aerosol-jet printing (UAJP) techniques typically handle inks with a viscosity < 30 cP.[43-45] The EG-based ink diluted with water with 1: 5.7 ratio, can also be easily printed via UAJP into high resolution patterns on 2D and 3D curved substrates (**Figure 5b**). As shown in **Figure 5c**, a 2D pattern with line width <0.1 mm was readily realized via a single printing pass. **Figure 5d** showed a 3D conformal architecture by printing MMC inks on a 3D hemisphere, which further confirms the high printability of MMC particles. While the detailed printed device performance is out of the scope of this article, the extrusion printed n-type $Bi_2Te_{2.7}Se_{0.3}$ film (24.7 μm in thickness) shows a room-temperature thermoelectric power factor of 662.9 μW m^{-1} K^{-2}, which is comparable to printed chalcogenide systems (**Figure 5e and Table S2**).[46-51] In future, device optimization and system integration would be desirable to complement the synthetic efforts to accelerate broad applications of semiconducting chalcogenide particles.

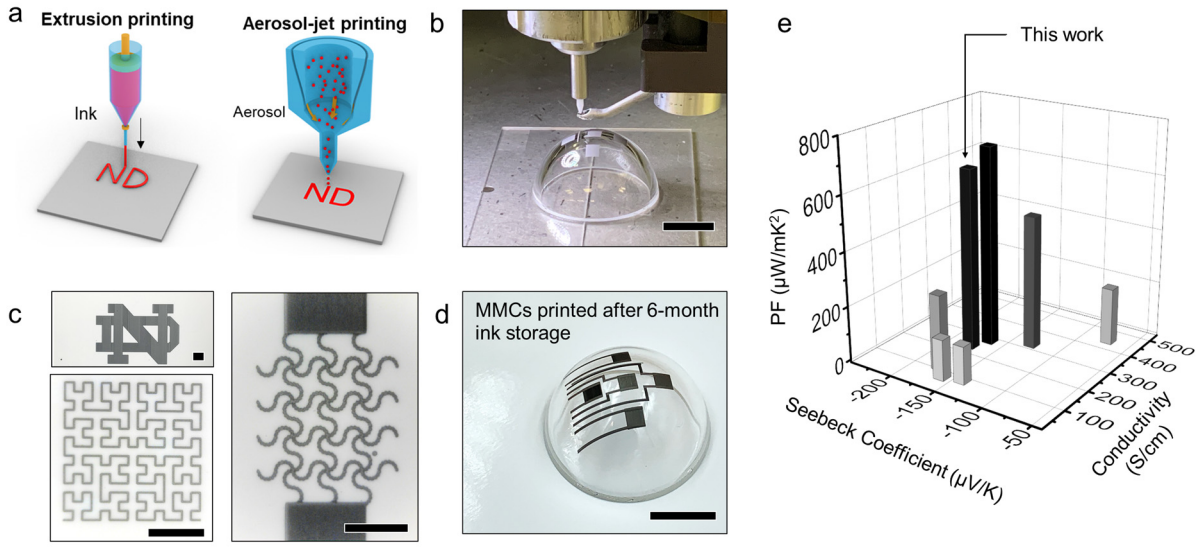

Figure 5. Ink printability of SCS synthesized MMCs. (a) Schematic illustration of two additive manufacturing processes including extrusion and aerosol jet printing. (b) Photographic image showing the aerosol jet printing process on a curved glass dome using MMC inks. Scale bar: 1 cm. (c) Several printed 2D patterns with high spatial resolution (as small as 50 μm in line width). Scale bars: 2 mm. (d) Photographic examples of 3D printed ternary chalcogenide nanoplates, showing excellent printability and processability even after 6-month ink storage. Scale bar: 1 cm. (e) Comparison of thermoelectric power factor of different printed n-type TE films (values from references [46-51]).

In summary, we investigated a hydrazine-free, phase-pure, and scalable approach for synthesizing and processing main group chalcogenides with an emphasis of V-VI nanoplates. We quantitatively compared the scale-up syntheses via hydrazine-based and hydrazine-free wet chemistry, and provided a systematic analysis on the scalability of chalcogenide synthesis. Upon scaling up the reaction, we observed the formation of byproduct tellurium during the MMC synthesis and correlated it with incomplete chalcogenide conversion. We demonstrated the role of applying classic Le Chatelier's principle and reaction kinetics in addressing the byproduct tellurium during the synthesis at a larger batch. By screening a number of ink factors including solvent, additives, and pH values, we investigated the effect of different ink formulations on MMCs and demonstrated a EG-based chalcogenide ink with long-term chemical stability at ambient environment. Combining highly scalable syntheses and judicious design of ink formulation could provide important insights toward large-scale applications of main group chalcogenide-based nanomaterials.

Methods

Materials. Sodium hydroxide, sodium tellurite, tellurium dioxide, selenium dioxide, antimony trichloride, bismuth(III) nitrate pentahydrate, polyvinylpyrrolidone (PVP, 40 000 g mol^{-1}), ethylene glycol, and diethylene glycol were obtained from Sigma-Aldrich (USA).

Hydrazine-based colloidal synthesis (HCS). Scale-up synthesis of MMCs nanoparticles were performed by strictly increasing the amount of starting materials 300% from our previous work.[21] In a typical synthesis of Sb_2Te_3, 210 mL ethylene glycol (EG) solution containing mixed antimony trichloride ($SbCl_3$, 18 mmol), tellurium dioxide (TeO_2, 27 mmol), sodium hydroxide (NaOH, 4.5 g), and PVP ($M_s \approx$ 40 000 g mol^{-1}, 2.4 g) were heated to 110 °C. 30 mL hydrazine hydrate was swiftly injected. The mixture was maintained at 130 °C for 30 min, and then heated under reflux for 12 h. The particles were collected by centrifugation at 5000 rpm, washed using ethanol for another three times.

Ethylene-assisted colloidal synthesis (ECS). In ECS method, there is no hydrazine involved during the entire synthesis process. In a typical synthesis of Sb_2Te_3, 210 mL ethylene glycol (EG) solution containing mixed antimony trichloride ($SbCl_3$, 18 mmol), tellurium dioxide (TeO_2, 27 mmol), sodium hydroxide (NaOH, 4.5 g), and PVP ($M_s \approx$ 40 000 g mol^{-1}, 2.4 g) was heated under reflux for 12 h. The particles were collected by centrifugation at 5000 rpm, washed using ethanol for another three times.

Solvent-engineered colloidal synthesis (SCS). The metal telluride particles were prepared by introducing a mixture of diethylene glycol and ethylene glycol. Taking the 300% scale-up synthesis of Sb_2Te_3 nanoplates for an example, antimony trichloride ($SbCl_3$, 18 mmol), sodium tellurite (Na_2TeO_3, 27 mmol), sodium hydroxide (NaOH, 5 g), and PVP ($M_s \approx$ 40 000 g mol^{-1}, 2.4 g) were added to 230 mL mixed solvent of ethylene glycol and diethylene glycol (1:2). The mixture was heated under reflux for 12 to 24 h. The particles were collected by centrifugation at 5000 rpm, washed using ethanol for another three times. For 300% scale-up synthesis of Bi_2Te_3 nanoplates, bismuth nitrate pentahydrate ($Bi(NO_3)_3 \cdot 5H_2O$, 18 mmol), sodium tellurite (Na_2TeO_3, 27 mmol), sodium hydroxide (NaOH, 5 g), and PVP ($M_s \approx$ 40 000 g mol^{-1}, 2.4 g) were added to 200 mL mixed solvent of ethylene glycol and diethylene glycol (4:1). The mixture was heated under reflux for 12 to 24 h. The particles were collected by centrifugation at 5000 rpm, washed using

ethanol for another three times. For synthesis of 1D tellurium nanowires, only sodium tellurite was used without the addition of antimony trichloride while keeping other conditions unchanged. In our experimental conditions, we found that the SCS method can be scale up to 54 mmol batch of metal precursors, which corresponds to the production of Sb_2Te_3 and Bi_2Te_3 are approximately 15 g and 20 g per batch, respectively.

Ink formulation. In a typical ink formulation, solvents, pH modifiers, and additives were used to formulate thermoelectric inks in 2 mL polypropylene tubes. For ink solvents, water and ethylene glycol were tested. For pH modifiers, 0.1 M HCl or 0.1 M NH_3 solution was added to inks to provide acidic or alkaline environment. Vitamin C (1 wt%) or ethyl gallate (1 wt%) was selected as oxygen scavengers in inks. The dispersion was sonicated using a bath sonicator for 15 min to ensure homogeneous dispersion of inks without aggregation. After a certain period of storage time, the chalcogenide particles were collected by centrifugation at 5000 rpm, washed using deionized water and ethanol for three times prior to resistivity measurements. The lateral size of the chalcogenide particles was characterized by SEM analyses. No aggregation was observed when the ink was transferred into the ink cartridge or during printing.

Printing, cold pressing, and sintering. In a typical printing process, we tested the printability of MMC inks using both aerosol jet printer and extrusion printer. For aerosol jet printing, an ultrasonic atomizer was used to aerosolize the ink which was then carried to the deposition head by an inert carrier gas flow (N_2). In the deposition head, the aerosolized ink flow is focused and directed to the substrate through a nozzle. Printing parameters are given in the supporting information (**Table S3**). For extrusion printing, a home-built printer with pneumatically controlled extrusion process was used. The extrusion apparatus mainly consists of ink cartridge and an extrusion needle of 22 gauge. To ensure the uniform density of the printed film, a systemic optimization of the extrusion pressure was performed ahead of printing the nanoplate ink. The approximate size of the printing was maintained at 15 mm × 2 mm with a 3.5 mm/s speed and 0.2 mm gap between adjacent layers. The printed TE film was completely dried in a furnace at 250 °C for 1 h prior to cold pressing twice at 20 MPa for 5 minutes. The dried and cold-pressed TE film is then sintered in an inert environment (N_2/H_2) at 450 °C for 1 h.

Characterization. A focused ion beam-scanning electron microscope (FIB-SEM, Helios G4 UX) was used to obtain SEM images of samples. Room temperature Seebeck coefficient and electrical conductivity are measured using a custom-built setup. We used the four-point probe method for electrical conductivity measurement. The printed TE film is placed on a dielectric substrate (glass slide) with two electrodes on both ends in which current is supplied for electrical conductivity measurement. We used high electrical conductivity silver adhesive (503 Electron Microscopy Sciences) for connecting current electrodes to the film. Two k-type thermocouples (40 AWG) are connected to the film using dielectric probes. The probes provide sufficient pressure on thermocouples (TCs) to maintain good contact between the TE film and TCs without causing any damage to the film. The voltage is measured across the negative leads of the thermocouples using a data acquisition system (Keysight 34970A). This is done for six equally spaced currents. The sample resistance R is the slope of the best fit line through the V/I data and the conductivity is then calculated as $\sigma = \frac{L}{RA}$, where L is the distance between the thermocouple tips and A is the cross-sectional area of the TE film. We used a 2D profilometer (DektakXT styles profilometer, Bruker, US) to measure the thickness of the film at five different locations and used the average value to calculate the cross-sectional area. For Seebeck coefficient measurement, one end of the film is placed on a heater and the other end on a heat sink. Temperature gradient ΔT is measured using TCs. Seebeck coefficient measurement begins by slowly ramping the temperature gradient ΔT from ~ 0 K to about 6 K while recording ΔT and voltage difference ΔV across the negative leads of the TCs using the data acquisition system. The negative of the slope of the best fit line through the ΔV/ΔT data gives the Seebeck coefficient relative to the material comprising the negative lead of the thermocouple ($S = \frac{-\Delta V}{\Delta T}$). The absolute Seebeck coefficient of the sample is obtained by adding the absolute Seebeck coefficient of the negative thermocouple wire material to the measured sample relative Seebeck coefficient. For Seebeck coefficient measurement, the instrument was calibrated using a standard constantan sample of known properties. The measurement error of the home-built set-up was ~5% for both the electrical conductivity and the Seebeck coefficient.

ACKNOWLEDGEMENTS. Y. Z. would like to acknowledge funding support from the National Science Foundation under award CMMI-1747685, and the U.S. Department of Energy under awards DE-EE0009103 and DE-NE0008812. At Northwestern work was supported mainly by the Department of Energy, Office of Science Basic Energy Sciences under grant DE-SC0014520, DOE Office of Science (TE measurements).

Competing interests: The authors declare no competing interests.

References

1. F. Kim, B. Kwon, Y. Eom, J. E. Lee, S. Park, S. Jo, S. H. Park, B.-S. Kim, H. J. Im, M. H. Lee, T. S. Min, K. T. Kim, H. G. Chae, W. P. King and J. S. Son, *Nature Energy*, 2018, **3**, 301-309.
2. S. Li, X. Li, Z. Ren and Q. Zhang, *Journal of Materials Chemistry A*, 2018, **6**, 2432-2448.
3. X. Wang, H. Wang, W. Su, T. Wang, M. A. Madre, J. Zhai, T. Chen, A. Sotelo and C. Wang, *Journal of Materials Chemistry A*, 2020, **8**, 3379-3389.
4. W. Zheng, T. Xie, Y. Zhou, Y. L. Chen, W. Jiang, S. Zhao, J. Wu, Y. Jing, Y. Wu, G. Chen, Y. Guo, J. Yin, S. Huang, H. Q. Xu, Z. Liu and H. Peng, *Nature Communications*, 2015, **6**, 6972.
5. F. Brückerhoff-Plückelmann, J. Feldmann, C. D. Wright, H. Bhaskaran and W. H. P. Pernice, *Journal of Applied Physics*, 2021, **129**, 151103.
6. J. Feldmann, N. Youngblood, M. Karpov, H. Gehring, X. Li, M. Stappers, M. Le Gallo, X. Fu, A. Lukashchuk, A. S. Raja, J. Liu, C. D. Wright, A. Sebastian, T. J. Kippenberg, W. H. P. Pernice and H. Bhaskaran, *Nature*, 2021, **589**, 52-58.
7. C. Han, Q. Sun, Z. Li and S. X. Dou, *Advanced Energy Materials*, 2016, **6**, 1600498.
8. Y. Zhang, S. Hao, L.-D. Zhao, C. Wolverton and Z. Zeng, *Journal of Materials Chemistry A*, 2016, **4**, 12073-12079.
9. H. Ju, D. Park and J. Kim, *Journal of Materials Chemistry A*, 2018, **6**, 5627-5634.
10. C. Zhou, Y. K. Lee, Y. Yu, S. Byun, Z.-Z. Luo, H. Lee, B. Ge, Y.-L. Lee, X. Chen, J. Y. Lee, O. Cojocaru-Mirédin, H. Chang, J. Im, S.-P. Cho, M. Wuttig, V. P. Dravid, M. G. Kanatzidis and I. Chung, *Nat Mater*, 2021, DOI: 10.1038/s41563-021-01064-6.
11. J. Fan, X. Wang, F. Liu, Z. Chen and G. Chen, *ACS applied materials & interfaces*, 2021, **13**, 30731-30738.
12. J. Fan, X. Huang, F. Liu, L. Deng and G. Chen, *Composites Communications*, 2021, **24**, 100612.
13. F. Rao, K. Ding, Y. Zhou, Y. Zheng, M. Xia, S. Lv, Z. Song, S. Feng, I. Ronneberger, R. Mazzarello, W. Zhang and E. Ma, *Science*, 2017, **358**, 1423.
14. M. Salinga, B. Kersting, I. Ronneberger, V. P. Jonnalagadda, X. T. Vu, M. Le Gallo, I. Giannopoulos, O. Cojocaru-Mirédin, R. Mazzarello and A. Sebastian, *Nature Materials*, 2018, **17**, 681-685.

15. W. Zhang and E. Ma, *Nature Materials*, 2018, **17**, 654-655.
16. C. Chen and J. Tang, *ACS Energy Letters*, 2020, **5**, 2294-2304.
17. M. Zeng, M. Chen, D. Huang, S. Lei, X. Zhang, L. Wang and Z. Cheng, *Materials Horizons*, 2021, DOI: 10.1039/D0MH01358G.
18. S. Bukkapatnam, S. Kamarthi, Q. Huang, A. Zeid and R. Komanduri, *IIE Transactions*, 2012, **44**, 492-495.
19. L. Xu, L. Wang and Q. Huang, *IIE Transactions*, 2015, **47**, 274-284.
20. C. Gu, H.-M. Xu, S.-K. Han, M.-R. Gao and S.-H. Yu, *Chem Soc Rev*, 2021, DOI: 10.1039/D0CS00881H.
21. C. Dun, W. Kuang, N. Kempf, M. Saeidi-Javash, D. J. Singh and Y. Zhang, *Advanced Science*, 2019, **6**, 1901788.
22. G. Zhang, W. Wang, X. Lu and X. Li, *Crystal Growth & Design*, 2009, **9**, 145-150.
23. H. Q. Yang, L. Miao, C. Y. Liu, C. Li, S. Honda, Y. Iwamoto, R. Huang and S. Tanemura, *ACS applied materials & interfaces*, 2015, **7**, 14263-14271.
24. R. Jin, G. Chen, J. Pei, H. Xu and Z. S. Lv, *Rsc Adv*, 2012, **2**, 1450-1456.
25. B. Zhou, Y. Ji, Y.-F. Yang, X.-H. Li and J.-J. Zhu, *Crystal Growth & Design*, 2008, **8**, 4394-4397.
26. K. Takahashi, S. Yokoyama, T. Matsumoto, J. L. Cuya Huaman, H. Kaneko, J.-Y. Piquemal, H. Miyamura and J. Balachandran, *New J Chem*, 2016, **40**, 8632-8642.
27. K. J. Carroll, J. U. Reveles, M. D. Shultz, S. N. Khanna and E. E. Carpenter, *The Journal of Physical Chemistry C*, 2011, **115**, 2656-2664.
28. J. Jiang, L. Chen, S. Bai, Q. Yao and Q. Wang, *Materials Science and Engineering: B*, 2005, **117**, 334-338.
29. M. Imamuddin and A. Dupre, *physica status solidi (a)*, 1972, **10**, 415-424.
30. D. McManus, S. Vranic, F. Withers, V. Sanchez-Romaguera, M. Macucci, H. Yang, R. Sorrentino, K. Parvez, S.-K. Son, G. Iannaccone, K. Kostarelos, G. Fiori and C. Casiraghi, *Nature nanotechnology*, 2017, **12**, 343.
31. T. Kalaivani, C. Rajasekaran and L. Mathew, *Journal of Food Science*, 2011, **76**, T144-T149.
32. S. Mohan, K. Thiagarajan and R. Chandrasekaran, *Biochemical Journal*, 2017, **474**, 3011-3025.
33. G. D. Cooper and J. G. Bennett, *The Journal of Organic Chemistry*, 1972, **37**, 441-447.
34. L. Panzella and A. Napolitano, *Antioxidants*, 2017, **6**, 30.
35. X. Lu, Q. Zhang, J. Liao, H. Chen, Y. Fan, J. Xing, S. Gu, J. Huang, J. Ma, J. Wang, L. Wang and W. Jiang, *Advanced Energy Materials*, 2020, **10**, 1902986.
36. Y.-W. Lai and W.-C. J. Wei, *Materials*, 2016, **9**, 863.
37. M. Zeng, S. A. Shah, D. Huang, D. Parviz, Y.-H. Yu, X. Wang, M. J. Green and Z. Cheng, *ACS applied materials & interfaces*, 2017, **9**, 30797-30804.
38. R. Ma, M. Zeng, D. Huang, J. Wang, Z. Cheng and Q. Wang, *J Colloid Interf Sci*, 2021, **601**, 106-113.
39. S. C. Bondy and S. Naderi, *Biochemical pharmacology*, 1994, **48**, 155-159.
40. H. M. Jalali, *Rsc Adv*, 2014, **4**, 32928-32933.
41. D. Chen, X. Qiao, X. Qiu and J. Chen, *Journal of Materials Science*, 2009, **44**, 1076-1081.
42. L.-J. Chen, C.-C. Wan and Y.-Y. Wang, *J Colloid Interf Sci*, 2006, **297**, 143-150.
43. M. Zeng and Y. Zhang, *Journal of Materials Chemistry A*, 2019, **7**, 23301-23336.

44. M. Zeng, W. Kuang, I. Khan, D. Huang, Y. Du, M. Saeidi-Javash, L. Zhang, Z. Cheng, A. J. Hoffman and Y. Zhang, *Adv Mater*, 2020, **32**, e2003081.
45. M. Saeidi-Javash, Y. Du, M. Zeng, B. C. Wyatt, B. Zhang, N. Kempf, B. Anasori and Y. Zhang, *ACS Applied Electronic Materials*, 2021, **3**, 2341-2348.
46. T. Varghese, C. Hollar, J. Richardson, N. Kempf, C. Han, P. Gamarachchi, D. Estrada, R. J. Mehta and Y. Zhang, *Scientific Reports*, 2016, **6**, 33135.
47. A. Chen, D. Madan, P. K. Wright and J. W. Evans, *Journal of Micromechanics and Microengineering*, 2011, **21**, 104006.
48. D. Madan, Z. Wang, A. Chen, R.-c. Juang, J. Keist, P. K. Wright and J. W. Evans, *ACS applied materials & interfaces*, 2012, **4**, 6117-6124.
49. M. Saeidi-Javash, W. Kuang, C. Dun and Y. Zhang, *Advanced Functional Materials*, 2019, **29**, 1901930.
50. S. Ferhat, C. Domain, J. Vidal, D. Noël, B. Ratier and B. Lucas, *Organic Electronics*, 2019, **68**, 256-263.
51. Y. Wang, G. Liu, M. Sheng, C. Yu and Y. Deng, *Journal of Materials Chemistry A*, 2019, **7**, 1718-1724.